JOURNAL OF GEOPHYSICAL RESEARCH, VOL. 97, NO. E12, PAGES 20,883–20,897, DECEMBER 25, 1992

Effects of Dispersed Particulates on the Rheology of Water Ice at Planetary Conditions

WILLIAM B. DURHAM

Lawrence Livermore National Laboratory, Livermore, California

STEPHEN H. KIRBY AND LAURA A. STERN

U.S. Geological Survey, Menlo Park, California

We have investigated the effects of initial grain size and hard particulate impurities on the transient and steady state flow of water ice I at laboratory conditions selected to provide more quantitative constraints on the thermomechanical evolution of the giant icy moons of the outer solar system. Our samples were molded with particulate volume fractions, ϕ, of 0.001 to 0.56 and particle sizes of 1 to 150 μm. Deformation experiments were conducted at constant shortening rates of 4.4×10^{-7} to 4.9×10^{-4} s^{-1} at pressures of 50 and 100 MPa and temperatures 77 to 223 K. For the pure ice samples, initial grain sizes were 0.2–0.6 mm, 0.75–1.75 mm, and 1.25–2.5 mm. Stress-strain curves of pure ice I under these conditions display a strength maximum σ_u at plastic strains $\varepsilon \leq 0.01$ after initial yield, followed by strain softening and achievement of steady state levels of stress, σ_{ss}, at $\varepsilon = 0.1$ to 0.2. Finer starting grain size in pure ice generally raises the level of σ_u. Petrography indicates that the initial transient flow behavior is associated with the nucleation and growth of recrystallized ice grains and the approach to σ_{ss} evidently corresponds to the development of a steady state grain texture. Effects of particulate concentrations $\phi < 0.1$ are slight. At these concentrations, a small but significant reduction in σ_u with respect to that for pure water ice occurs. Mixed-phase ice with $\phi \geq 0.1$ is significantly stronger than pure ice; the strength of samples with $\phi = 0.56$ approaches that of dry confined sand. The magnitude of the strengthening effect is far greater than expected from homogeneous strain-rate enhancement in the ice fraction or from pinning of dislocations (Orowan hardening). This result suggests viscous drag occurs in the ice as it flows around the hard particulates. Mixed-phase ice is also tougher than pure ice, extending the range of bulk plastic deformation versus faulting to lower temperatures and higher strain rates. The high-pressure phase ice II formed in $\phi = 0.56$ mixed-phase ice during deformation at high stresses. Bulk planetary compositions of ice + rock ($\phi = 0.4$–0.5) are roughly 2 orders of magnitude more viscous than pure ice, promoting the likelihood of thermal instability inside giant icy moons and possibly explaining the retention of crater topography on icy planetary surfaces.

INTRODUCTION

We have extended our laboratory study of the flow and fracture of water ice I [*Durham et al.*, 1983; *Kirby et al.*, 1987] to include ice + rock mixtures. Water is one of the more important volatile constituents of many of the low-density moons of the outer solar system, and since most of these moons have some rocky component, ice + rock mixtures must exist or have existed in at least some regions on these moons. Our experiments are intended to constrain evolutionary models of the icy moons. Of particular interest is the so-called Ganymede-Callisto dichotomy, which has puzzled planetologists since the Voyager flybys of Jupiter; although the two giant moons have nearly identical compositions, they have radically different external appearances [*McKinnon and Parmentier*, 1986; *Mueller and McKinnon*, 1988]. The difference between the moons may have resulted from a thermomechanical instability during the evolutionary process. *Friedson and Stevenson* [1983] have suggested that subtle differences in ice/rock ratios can produce rheological differences that can drive an icy moon to differentiate (Ganymede?) or not differentiate (Callisto?).

The determination of the rheology of ice + rock mixtures is also crucial to understanding the nature of planetary surfaces, particularly regarding viscous relaxation of craters and other topographic features. The surface layer is plausibly rich in rocky material because it has remained sufficiently cold to prevent differentiation by melting and because it contains rocky dust that continuously rains down on surfaces. Varying ice/rock ratios are often cited as explanations for strong variations in albedo of icy satellites (see, e.g., *McKinnon* [1985] for a more detailed review of these topics). Knowledge of the rheology of ice + rock mixtures may eventually help constrain surface compositions, although interpreting viscously relaxed crater shapes is currently controversial: some models of crater relaxation using our flow laws for pure ice suggest that pure ice I is too weak to support current crater topography [*Croft*, 1988; *Thomas and Schubert*, 1988], while others suggest that observed crater topography is compatible with pure ice rheology [e.g., *Schenk*, 1991; *Hillgren and Melosh*, 1989]. *Geissler and Croft* [1988] and *Thomas and Schubert* [1988] argue that silicate particles can harden ice through the process of dispersion hardening. Dispersed particles harden the material by pinning glide dislocations and forcing them to climb over obstacles or to bow and pass around them.

The purpose of the present study is to investigate the effects of hard particulates on the flow of ice I at conditions appropriate to the surfaces and interiors of large icy moons. Our results from several related studies, which have helped us interpret the results of this investigation of the effect of

Paper number 92JE02326.
0148-0227/92/92JE-02326$05.00

particulates, are presented here also. Those related studies are (1) a refinement of the flow law for pure ice I, which was necessary to improve the resolution of some of the more subtle effects of particulates; (2) the effect of varying initial grain size in pure ice I; and (3) a microstructural study of textural evolution during the initial stages of deformation.

SAMPLE FABRICATION

Our test specimens are fully dense cylinders of polycrystalline ice mixed with solid particulates. The test cylinders measured 25 mm in diameter and 63 mm in length and had the following ranges of particulate loading, stated in terms of volume fraction ϕ: $\phi = 0.001 \pm 0.0002$ SiC, $\phi = 0.20 \pm 0.02$ $CaCO_3$, and $\phi = 0.10 \pm 0.01$, 0.30 ± 0.02, and 0.56 ± 0.01 SiO_2.

We manufactured the samples by adapting a method we described earlier [*Durham et al.*, 1983], and we briefly outline here. Sieved seed ice grains, made by grinding frozen distilled water in a blender, were packed into stainless steel tube molds to a standard porosity of 40%. The molds were then evacuated at about 258 K to a pressure near 10^{-3} atm for 15 min. While still under vacuum, the molding assembly was immersed in a water/ice bath. When the assembly had equilibrated at 0°C, distilled water, degassed by boiling and cooled under its own vapor to 0°C, was admitted to the molding chamber and after several seconds, air pressure was opened above the water source, further driving the water into the molds. The individual molds were then placed on a copper plate in a freezer at 255 to 258 K while covered on the sides and top by foam insulation. Freezing thus proceeded upward over the course of several hours, driving any exsolved gas bubbles ahead of the freezing front, eventually leaving them near the top of the sample where they could be cut off and discarded after freezing was complete. The polycrystalline ice that results has a uniform texture, and the grains show no preferred orientation, are equant, and lack optical evidence of internal strain (Figure 1*a*). Our "standard" ice we routinely use for experimental starting material is made from 0.6- to 1.0-mm seed ice, and further grain growth yields a final grain size of 0.75–1.75 mm. Other pure ice samples fabricated for this study were made with 180- to 250-μm and 1- to 2-mm seed ice, yielding samples with final grain sizes of 0.2–0.6 mm and 1.25–2.5 mm, respectively.

The mixed-phase ice samples were made by mixing the seed ice with weighed amounts of particulates at 255–258 K until a uniform appearance was obtained and then packing this mixture into the molds to a standard porosity of 40%. Three different particulates were used: 20-μm SiC, 2 ± 1-μm calcite, and 100 ± 50-μm quartz sand. Subsequent steps were identical to those described above for the pure ice samples, except that the samples with the highest volume concentration of quartz sand ($\phi = 0.56$) were made by packing the molds with pure sand without seed ice. Although we made some of our earliest SiC + ice aggregates by freezing water with SiC and then grinding and sieving this aggregate for seed material, the test results of these samples were indistinguishable from those of samples made by the more conventional method.

The resultant samples are not uniformly dispersed aggregates of ice and particles. The uniformity of SiC particulates in the ice samples is good, based on external examination of the transparent ice samples. The same is not true of the calcite + ice samples. Replicas of the surfaces of sawcut and polished samples (Figure 1*b*) show approximately spherical ice grains (with some fine inclusions of calcite) immersed in an aggregate of concentrated calcite and ice. Several large ice grains contain fine calcite rings delineating the original seed ice grain, suggesting that most of the calcite is excluded during continued growth of the ice grains. This presumably occurs because of surface tension at the liquid-ice interface

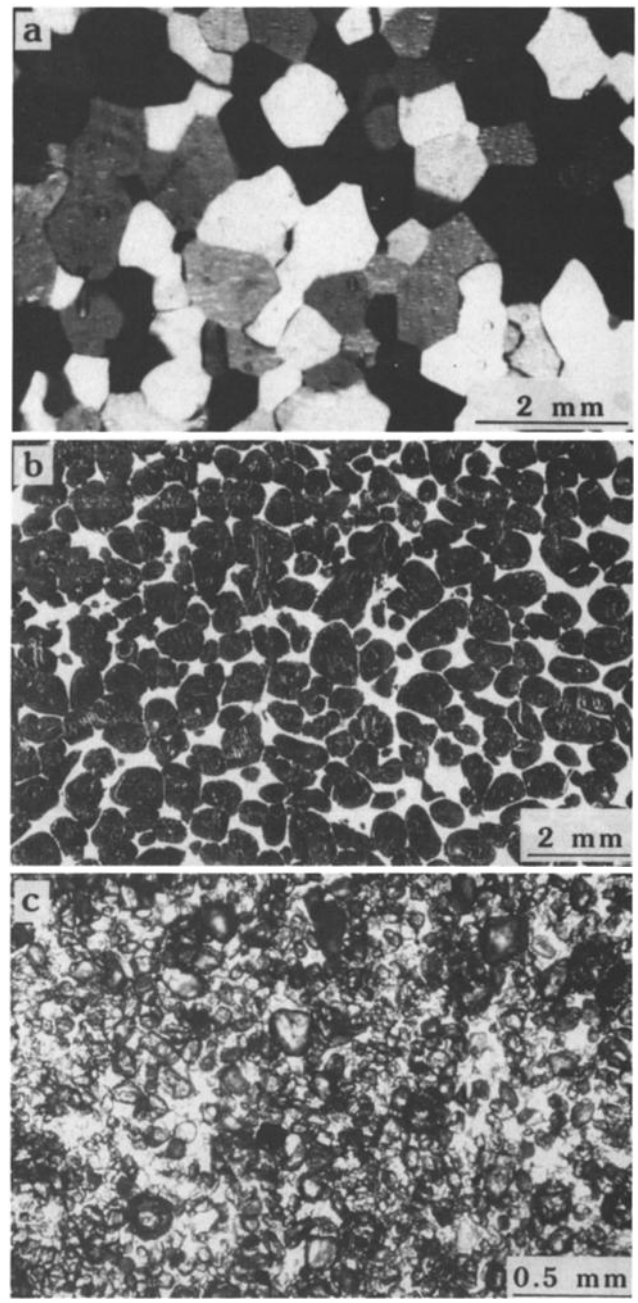

Fig. 1. Micrographs of thin sections and replicas of the starting material. (*a*) "Standard" ice of 0.75–1.75 mm starting grain size, showing equant, randomly oriented grains and no intergranular porosity. (*b*) Ice + 20 vol % calcite. The calcite has been preferentially swept into a network along the boundaries of ice grains (which appear here has dark, rounded grains) that are nearly calcite-free. (*c*) Ice + 56 vol % quartz showing uniform particulate distribution. The grains in this micrograph are quartz; individual ice grains are not apparent.

and the volume increase upon freezing that squeezes the remaining calcite-water mixture and expels excess water through the porosity into the water reservoir in the molds above the sample chamber. Particulates in $\phi = 0.10$ and 0.30 quartz sand + ice samples appear to be somewhat more uniformly distributed than in the calcite + ice samples, but this may largely be due to the difference in particulate sizes. The quartz particulates are 100X larger than the calcite particulates, giving the quartz-bearing samples a significantly coarser appearance. For quartz + ice samples with $\phi = 0.10$ and 0.30, the texture, similar to calcite + ice samples, is dominated by seed ice plus an interstitial ice/particulate mix. This agrees with *Baker*'s [1978] observation that when using a freezing process similar to ours, quartz sand particles also tend to be attracted to liquid/solid interfaces and subsequently end up in grain boundaries. Our highest concentration quartz/ice samples ($\phi = 0.56$), however, have a very uniform quartz distribution, since no seed ice was involved in the fabrication process (Figure 1*c*). The ice grains in these samples grew to an average size of 0.4–1.0 mm, often encompassing the dispersed quartz grains.

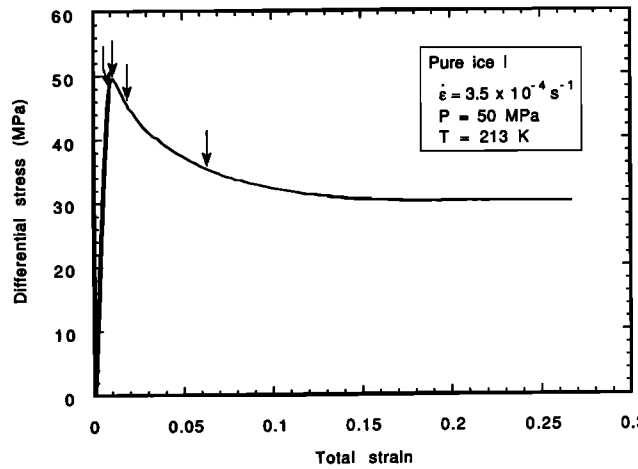

Fig. 2. A typical stress-strain curve for pure ice at 213 K and 3.5×10^{-4} s^{-1}. The curve is actually a composite of several runs that were stopped at various strains (indicated by the arrows) to allow microstructural examination. Micrographs at each of the arrows are shown in Figures 10*a*–10*d*. "Total strain" on the horizontal axis is elastic strain plus permanent strain.

Experimental Methods

Samples were sealed in indium metal jackets to exclude the confining pressure medium and mechanically tested at elevated pressure and low temperature using techniques that have been described elsewhere [*Durham et al.*, 1983; *Heard et al.*, 1990] and are only summarized here. The testing apparatus is a conventional high-pressure gas vessel outfitted with a sliding piston that loads the end of the sample in compression. The usual mode of operation is constant-displacement-rate testing, wherein the dependent variable, the force F above hydrostatic required to keep the sample shortening at a constant displacement rate $\dot{u}$, is measured by an internal force gauge. The vessel is immersed in a liquid-filled cryostatic tank and can be chilled to temperatures as low as 77 K. Temperature stability is usually excellent, ±0.5 K or better, because of the large thermal inertia of the system.

"Standard" relationships and conventions are used to convert measured quantities F, $\dot{u}$, and shortening displacement Δu to differential stress (σ), strain rate $\dot{\varepsilon}$, and shortening strain ε:

$$\varepsilon = \Delta u / L_0$$

$$\dot{\varepsilon} = \dot{u}/L$$

$$\sigma = F/A$$

where L_0 is the starting sample length measured along the cylinder axis, and L and A are the instantaneous sample length and area normal to the cylinder axis, respectively. The value A follows from the assumption of uniform strain and constant sample volume.

In the ductile field, the deformation of ice can usually be described by a relationship of the form

$$\dot{\varepsilon}_{ss} = A \sigma_{ss}^{n} e^{-(Q^* + PV^*)/RT} \quad (1)$$

where P is pressure, T is temperature, and A, n, Q^*, and V^* are constants. R is the gas constant. The subscript ss refers to "steady state," which in this paper is taken to mean that the variable in question does not change in an increment of time.

Many figures in this paper are Arrhenius diagrams of log σ_{ss} versus inverse temperature at conditions of fixed pressure and strain rate. However, under the experimental condition of constant displacement rate, strain rate is slightly strain-dependent, so to plot results at constant strain rate, we correct σ_{ss} on the basis of (1) by an amount $(\dot{\varepsilon}/\dot{\varepsilon}_0)^{1/n}$, where $\dot{\varepsilon}_0$ is the fixed strain rate. The exact value of n is unknown before testing, of course, so an iterative exercise is necessary for the exact correction. In practice, however, the strain rate correction is small enough that approximate values of n are satisfactory. Here we use $n = 5$. The nominal strain rate $\dot{\varepsilon}_0$ we use in the figures is 3.5×10^{-m} s^{-1}, where m is a positive integer, while the actual $\dot{\varepsilon}$ ranges from about 3.3 to 4.9×10^{-m} s^{-1}. The change in σ_{ss} corresponding to a ±1 change in n is about 2%.

Figure 2 shows a "typical" stress-strain curve for polycrystalline ice in a constant-strain-rate test. Following an initial linear quasi-elastic response, we observe a yield deflection from linearity. A strength maximum is then reached at a level we label σ_u (the ultimate strength). The material strain softens over the next several percent, depending on strain rate and temperature, and finally reaches the steady state level σ_{ss}. Many runs in this study are simple, one-condition runs, but several are strain-rate-stepping or temperature-stepping experiments wherein external conditions are changed after the initial achievement of steady state.

Results and Discussion

Thirty-four samples were tested in 36 runs. Test temperatures ranged from 77 K to 223 K and strain rates from 4.37×10^{-7} to 4.85×10^{-4} s^{-1}. Most of the tests were done at a confining pressure of 50 or 100 MPa. Eighteen samples (20 runs) were ice I plus particulates; 16 samples (16 runs) were pure ice I. Mechanical data for the experiments are listed in Tables 1 and 2.

To summarize the results, the effect of low concentrations

TABLE 1. Deformation Data for Ice I + Particulates

Run	Sample	P, MPa	T, K*	ε	$\dot{\varepsilon}$, s^{-1}	σ_u, MPa	σ_{ss}, MPa
180	SiC	50	223	0.210	4.33×10^{-4}	34.6	21.6
		50	223	0.281	4.72×10^{-5}		14.0
181	SiC	50	223.5	0.217	4.38×10^{-4}	35.4	20.6
		50	223.5	0.292	4.78×10^{-5}		13.2
182	SiC	50	222.8	0.216	4.37×10^{-4}	34.2	20.2
		50	222.8	0.290	4.80×10^{-5}		12.8
186	SiC	50	224	0.211	4.35×10^{-4}	33.9	19.9
		50	224	0.286	4.78×10^{-5}		12.8
194	20% $CaCO_3$	50	222.9	0.304	4.90×10^{-4}	31.7	22.1
207	20% $CaCO_3$	50	178.9 ± 0.7	0.209	4.13×10^{-5}	82.3	53.4
208	20% $CaCO_3$	50	179.4	0.194	4.06×10^{-6}	48.4	37.1
215	20% $CaCO_3$	50	179.0 ± 1	0.139	3.80×10^{-4}	106.7	78.4
		50	179.0 ± 1	0.311	4.75×10^{-6}		33.9
217	20% $CaCO_3$	50	159.2	0.115	3.70×10^{-5}	116.9	100.3
		50	159.2	0.174	3.97×10^{-6}		69.6
		35.5	159 ± 1	0.283	4.57×10^{-7}		46.0
		50	159 ± 1	0.305	4.71×10^{-5}		91.5
232	56% SiO_2	50	223	0.007	3.41×10^{-4}	50.9	
		50	223	0.113	3.81×10^{-5}		49.4
		50	223	0.165	4.05×10^{-4}		70.0
		50	223	0.225	4.37×10^{-5}		53.2
234	56% SiO_2	100	183	0.147	3.86×10^{-5}	93.9	119.9
		100	162	0.257	4.43×10^{-5}		136.8
235	10% SiO_2	100	180	0.086	3.62×10^{-5}	74.9	59.3
		100	180	0.138	3.84×10^{-4}		84.0
		100	180	0.182	4.04×10^{-5}		56.2
		100	179.5	0.225	4.27×10^{-6}		40.5
		100	179.5	0.260	4.47×10^{-5}		60.8
240	10% SiO_2	100	161	0.093	3.67×10^{-5}	108.0	85.8
241	30% SiO_2	100	223	0.057	3.53×10^{-4}	38.9	34.2
		100	223	0.109	3.74×10^{-5}		23.6
244	10% SiO_2	100	223	0.097	3.67×10^{-4}	35.7	26.4
		100	223	0.122	3.77×10^{-6}		10.4
		100	203	0.180	4.03×10^{-5}		32.6
246	30% SiO_2	100	77	0.016	3.42×10^{-4}	189.7 (faulted)	
250	30% SiO_2	100	77	0.009	3.78×10^{-4}	151.6 (faulted)	
251	56% SiO_2	100	77	0.009	3.35×10^{-6}	119.4 (faulted)	
252	10% SiO_2	see run 244					
		100	142 ± 2	0.175	4.01×10^{-6}		141.0
		100	161 ± 1	0.199	4.13×10^{-6}		83.8
		100	183	0.228	4.29×10^{-6}		40.9
		100	168	0.250	4.41×10^{-6}		66.0
		100	160.5	0.270	4.53×10^{-6}		83.6
253	56% SiO_2	see run 232					
		100	160.5	0.228	4.38×10^{-6}		157 ± 9
		100	170	0.258	4.56×10^{-6}		142.5
		100	182.5	0.277	4.68×10^{-6}		112.6
		100	202	0.302	4.85×10^{-6}		73.3

*Precision plus fluctuations is ±0.5 K except as noted. Accuracy is an additional ±1 K.

of particulates on the strength of ice I, as well as the effect of varying initial grain size, is small and mainly confined to the transient portion of the stress-strain curve. On the other hand, the effect of particulates in volume concentrations $\phi \geq 0.10$ is a strengthening that increases rapidly with particulate concentration. Particulate concentrations $\phi \geq 0.10$ also toughen ice, extending the range of bulk plastic deformation versus faulting to lower temperatures and higher strain rates.

Microstructural observation of thin sections and jacket replicas have provided further insight and are presented and discussed in a later section.

Comparison of transient effects. We directly compared the effects of varying grain size and particulates at three temperatures, 223 K (Figure 3), 180 K (Figure 4), and 160 K (Figure 5). The transient phenomenon wherein strain softening follows initial yielding seems to be a universal feature of the topology of stress-strain curves in ice. The shape of this yield phenomenon apparently can be affected by impurities and initial grain sizes, but in a previously undeformed sample it is always present. It has been our experience that the transient behavior of pure ice is difficult to reproduce (compare "standard" ice runs 188 and 189, Table 2 and Figure 3), so it is noteworthy that the four SiC + ice samples deformed in this study produced virtually identical stress-strain curves (compare the first four runs in Table 1); the one SiC curve in Figure 3 applies to those runs. This reproducibility is even more remarkable given the fact that the four samples, although they contained the same amount of SiC, were prepared from two different seed sizes (0.6–1 mm and 0.25–0.6 mm) as well as two different seed compositions (pure ice and ice + SiC). Simply varying the size of the seed grains seems to have more of an effect in pure ice samples. The unusually good reproducibility suggests that the SiC particles provide nucleation points for the recrystallization

TABLE 2. Deformation Data for Water Ice of Varying Initial Grain Size

Run	Sample	P, MPa	T, K*	ε	$\dot{\varepsilon}$, s^{-1}	σ_u, MPa	σ_{ss}, MPa
90	GS 0.6–1.0 mm	100	213	0.009	3.29×10^{-4}	48.4	
91	GS 0.6–1.0 mm	100	213	0.007	3.30×10^{-4}	>49.9	
93	GS 0.6–1.0 mm	100	213	0.057	3.40×10^{-4}	50.8	<30.4
94	GS 0.6–1.0 mm	100	213	0.017	3.28×10^{-4}	46.2	
188	GS 0.6–1.0 mm	50	222.7	0.216	4.36×10^{-4}	36.8	20.1
		50	222.7	0.288	4.79×10^{-5}		13.2
189	GS 0.6–1.0 mm	50	222.6	0.220	4.37×10^{-4}	28.2	19.7
		50	222.6	0.295	4.85×10^{-5}		12.9
192	GS 1–2 mm	50	222.8	0.237	4.47×10^{-4}	36.0	22.3
193	GS 180–250 μm	50	222.8	0.275	4.72×10^{-4}	33.6	20.5
195	GS 180–250 μm	50	179.2	0.169	4.14×10^{-5}	87.8	49.8
197	GS 1–2 mm	50	179.2 ± 0.7	0.151	4.01×10^{-5}	81.1	64.0
205	GS 1–2 mm	50	179.6	0.187	4.03×10^{-6}	54.8	36.5
206	GS 0.6–1.0 mm	50	179.5	0.193	4.08×10^{-6}	60.7	32.9
210	GS 180–250 μm	50	179.4	0.195	4.07×10^{-6}	58.3	28.8
211	GS 0.6–1.0 mm	50	179.0 ± 1	0.141	3.83×10^{-4}	105.7	73.7
		50	179.2 ± 1	0.252	4.40×10^{-5}		46.6
		50	179.2 ± 1	0.310	4.77×10^{-6}		28.6
212	GS 180–250 μm	50	179.2 ± 1	0.140	3.82×10^{-4}	112.7	74.3
		50	179.3	0.248	4.37×10^{-5}		44.5
		50	179.0 ± 1	0.308	4.75×10^{-6}		28.3
216	GS 0.6–1.0 mm	50	159.0 ± 1	0.117	3.73×10^{-5}	119.6	93.0
		50	159.0 ± 1	0.172	3.97×10^{-6}		65.3
		50	159.0 ± 1	0.248	4.37×10^{-7}		41.4
		50	159.0 ± 1	0.270	4.50×10^{-5}		86.9

*Precision plus fluctuations is ±0.5 K except as noted. Accuracy is an additional ±1 K.

that is believed to control both yield and steady state flow at this temperature [*Kirby et al.*, 1987]. The role of recrystallization during yield is discussed further under section of microstructural studies below.

The effect of higher amounts of particulates is generally to suppress the magnitude of the drop in stress $\sigma_u - \sigma_{ss}$ after yield. The above mentioned scatter in the transient behavior of ice may obscure the effect in certain instances, but in the majority of side-by-side comparisons that can be made in Figures 3–5, the calcite + ice and quartz + ice samples have

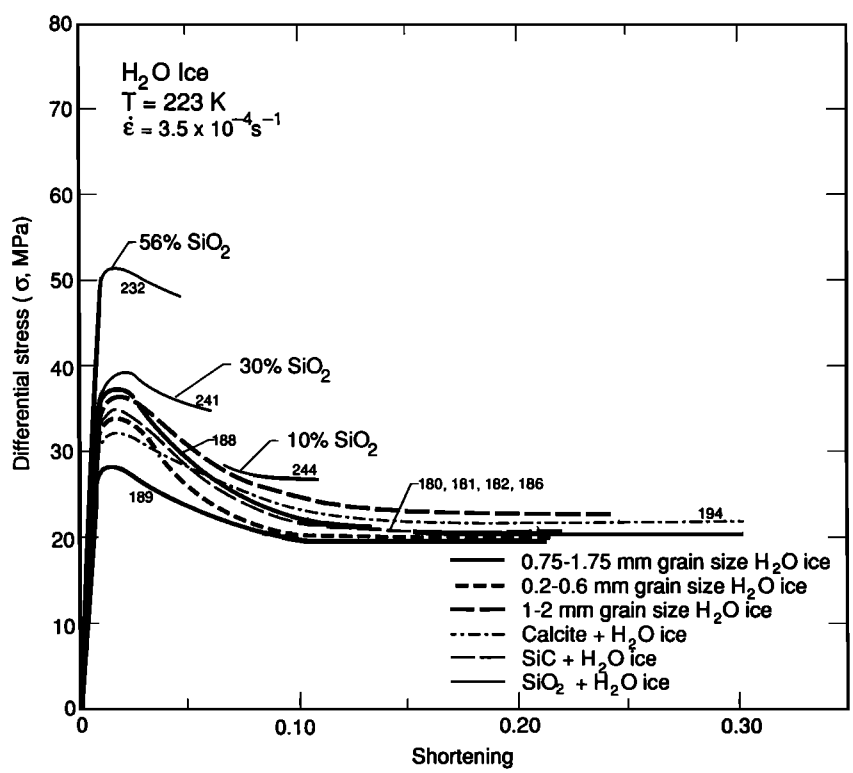

Fig. 3. A comparison of run records for samples deformed at 223 K and a strain rate of 3.5×10^{-4} s^{-1}. Data are corrected for sample area and length changes. Each curve is labeled with its run number.

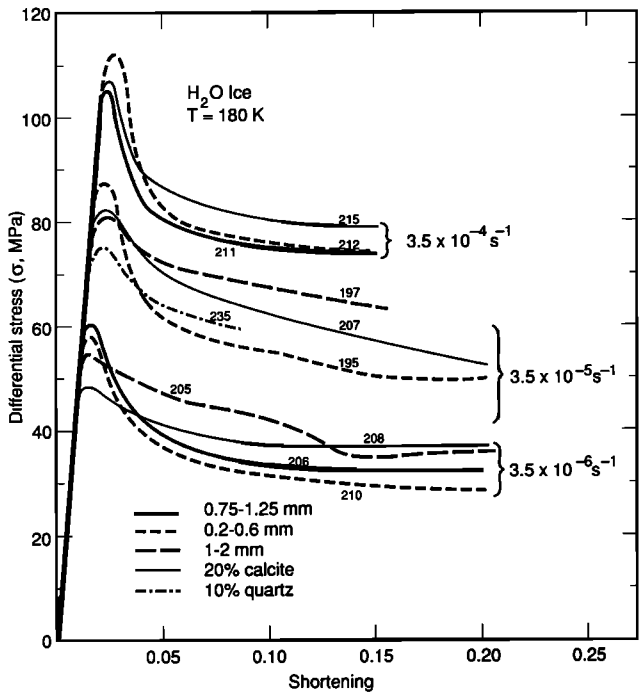

Fig. 4. A comparison of run records for samples of calcite + ice, quartz + ice, and varying-grain-size ice at 180 K and three different strain rates. Each curve is labeled with its run number. Calcite + ice may be slightly stronger at the steady state level than the other ices, and ice with the finest grain size may have a slightly higher maximum stress than the other materials.

a comparatively smaller value of σ_u than pure ice. There may also be an effect related to grain size in pure ice, but it is even harder to see in the scatter. The size of the stress drop in fine-grained ice at the two highest strain rates at T = 180 K (Figure 4) is unusually large. However, at lower strain rates (Figure 4) and higher temperature (Figure 3) the stress drop in fine-grained ice is normal.

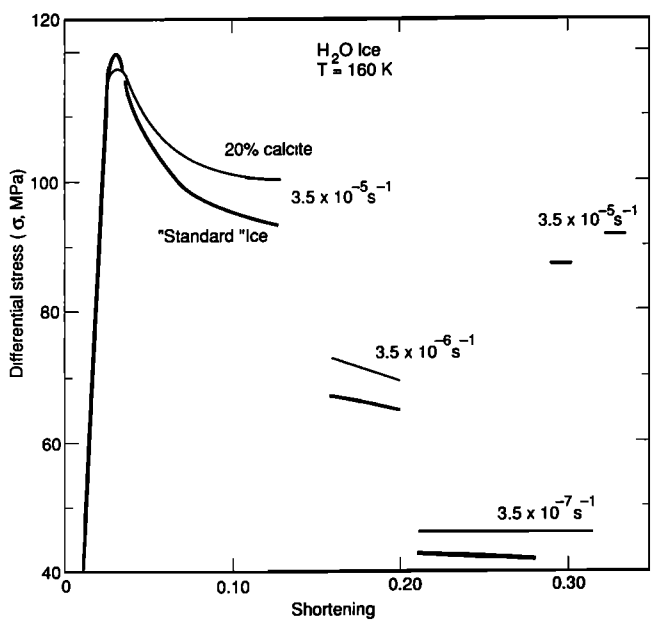

Fig. 5. Side-by-side comparison at 160 K of sequential runs 216 and 217, showing a subtly but consistently higher strength for calcite + ice than for "standard" ice, although the standard ice has a slightly higher maximum strength at yield.

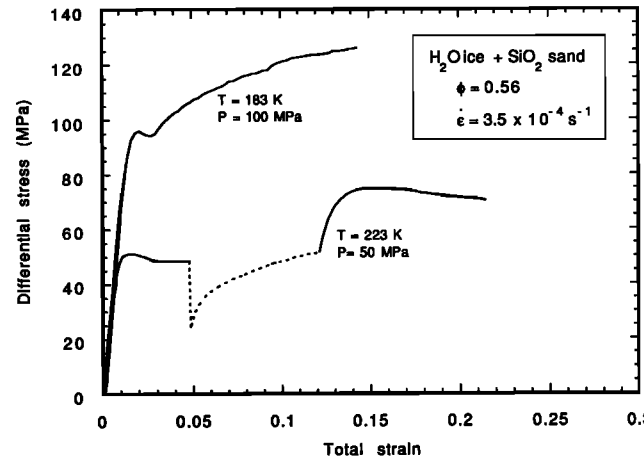

Fig. 6. Stress-strain curves for the two $\phi = 0.56$ quartz samples deformed in this study. The dashed portion of the lower curve was a deformation step at a strain rate 10 times lower. The distinct strengthening following initial yield is unique to these two samples and suggests direct contact between the quartz particles. The difference in the (approximately) steady state portion of the curves may be partially influenced by the difference in confining pressures (see text).

Higher charges of quartz sand ($\phi \geq 0.3$) clearly raise the level of σ_u (Figure 3). At the highest charges a unique yield phenomenon occurs (Figure 6 and Table 1, runs 232 and 234, $\phi = 0.56$ quartz). In those runs an initial strength maximum was followed by a brief period of strain softening, after which there occurred an extended period of strain hardening. Since $\phi = 0.56$ is close to the densest packing of particles of uniform size, it is reasonable to suspect that narrow ice "bridges" between the hard particulates closed after a small amount of strain; the hard particles then contacted and formed a rigid framework, causing the stress to rise again after the first stress maximum. Similar behavior has been observed by *Parameswaren and Jones* [1981] in frozen sand deformed at 263 K. Although their samples were unjacketed, causing failure after a few percent strain, they also concluded that the second rise of strength with strain was caused by sand particles coming in contact with each other.

Comparison of "steady state" ductile strengths. The flow law for "standard ice," pure ice I of grain size 0.75–1.75 mm, serves as a useful datum for comparison to other ices. However, there is some uncertainty in the location of this datum, especially at $T < 200$ K. This uncertainty is illustrated in Figure 7 where our earlier data [*Kirby et al.*, 1987] are compared with standard ice tested as a part of this study (Table 2). At $T > 195$ K the agreement between earlier and more recent results is good; at $T < 195$ K the more recent results are consistently lower than the earlier results by a factor of about 1.5, or about one order of magnitude in strain rate at fixed stress. We were aware of this discrepancy during the tests but still were unable to determine the cause. A measurement error is very unlikely. Force gauge calibrations have been in good order throughout the history of this apparatus and in fact have shown no drift over several years. The several thermocouples used on the system since about

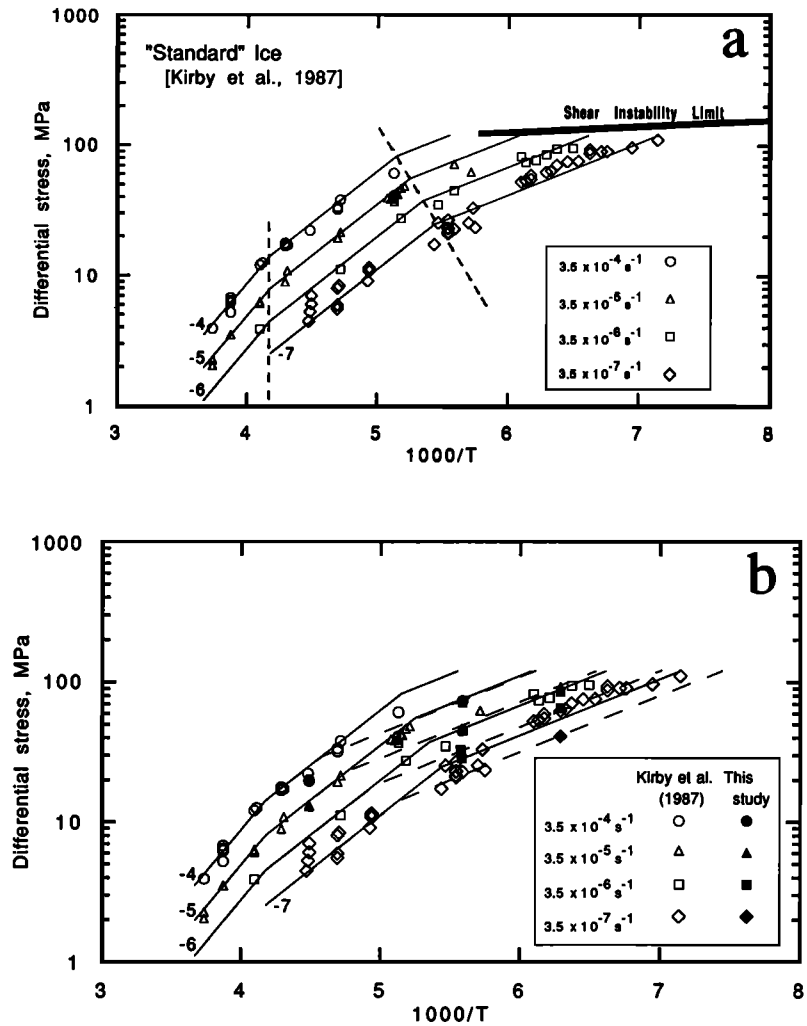

Fig. 7. Flow of "standard" ice (grain size 0.75–1.75 mm) at a confining pressure of 50 MPa. (*a*) Results reported by *Kirby et al.* [1987], redrawn here with a more complete data set. The lighter solid lines are the flow laws given in Table 3 and by Kirby et al. for the four values of strain rate listed in the legend. The lines are labeled with the appropriate power of 10 strain rate exponent. The short-dashed lines delimit the regions of dominance of three different flow mechanisms. Plastic flow can apparently not be achieved under any conditions above the "shear instability limit." (*b*) Results of the present work (solid symbols) combined with those from Figure 7*a* (open symbols), showing a viscosity approximately one order of magnitude lower for temperatures below 195 K. The solid lines are the flow laws in Figure 7*a*. The long-dashed lines are an estimated fit to the new data, with constants given in Table 3.

midway through the earlier tests have not been changed, and no change in the temperature distribution (which at $T > 158$ K, the freezing temperature of the ethanol bath, is nearly flat) has occurred. Nor has there been any obvious change in the raw materials used to make samples or in the sample fabrication procedure. The starting grain size and orientation have not changed, as documented in thin sections.

The difference in the flow laws is significant, falling outside the range of parameters given by *Kirby et al.* [1987] (also Table 3). For the purposes of this work, we have estimated a second set of parameters for the low-temperature flow regime. We leave unresolved the question of which set of parameters is more appropriate, say, to flow within the icy moons.

TABLE 3. Flow Parameters for Ice I at a Confining Pressure of 50 MPa

T Range, K	$\log_{10}A$, $MPa^{-n}\ s^{-1}$	n	Q^*, kJ/mol	V^*, m^3/mol	Reference
240–258	11.8 ± 0.4	4.0 ± 0.6	91 ± 2	···	*Kirby et al.* [1987]
~195–240	5.10 ± 0.03	4.0 ± 0.1	61 ± 2	$-13 \pm 3 \times 10^{-6}$	*Kirby et al.* [1987]
<195	−2.8 ± 0.6	4.7 ± 0.3	36 ± 5	···	*Kirby et al.* [1987]
<195†	−1.4	5.6	43	···	this study (Figure 7*b*)

†Data too sparse to estimate uncertainties. Assume they are at least as large as for *Kirby et al.* [1987].

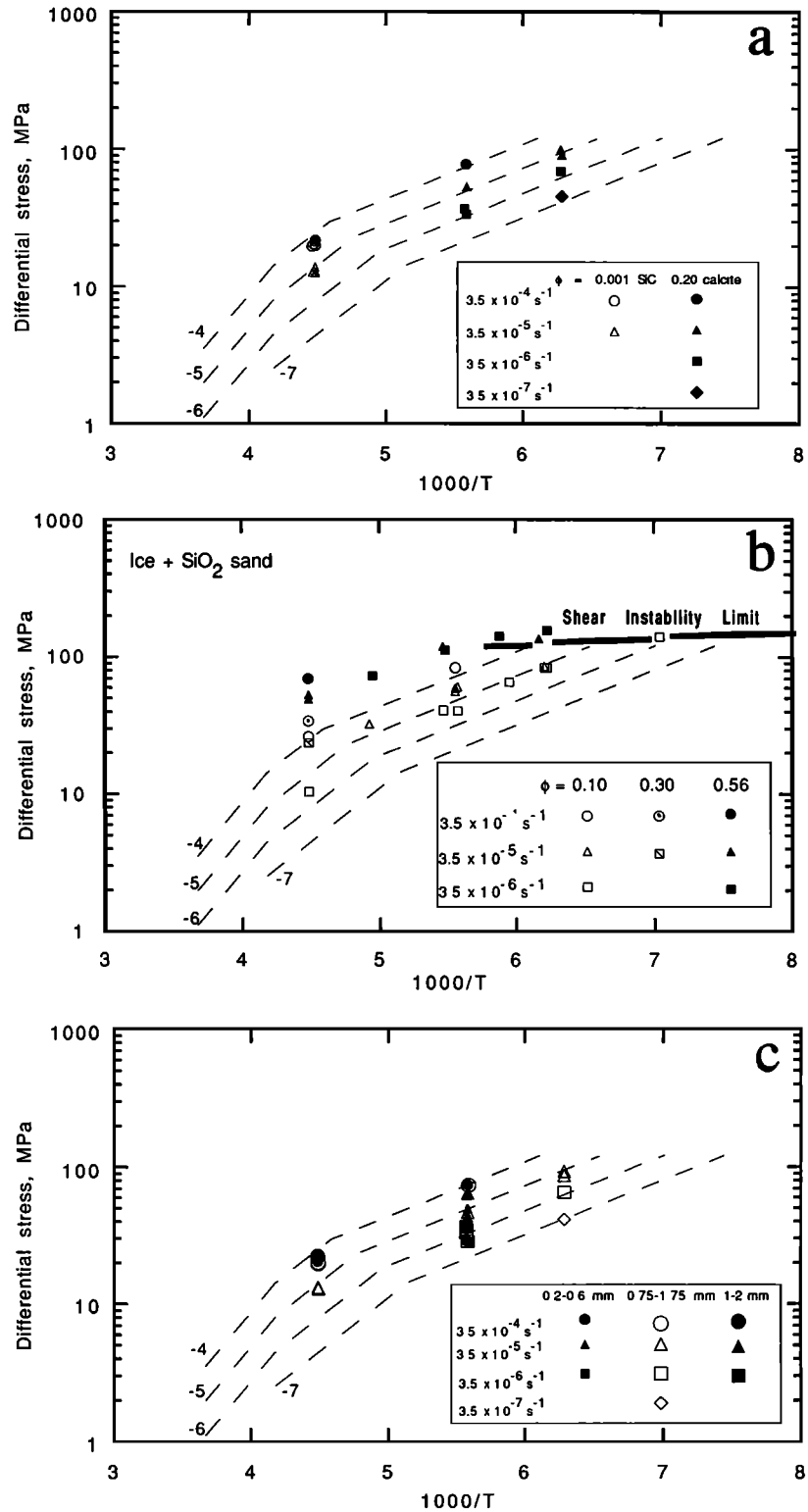

Fig. 8. Steady state flow data for (*a*) ice + SiC or calcite, (*b*) ice + quartz sand, and (*c*) ice of varying initial grain size. Dashed lines are the pure ice flow laws taken from Figure 7*b*. Exponent labels on lines indicate appropriate strain rate.

Because of this problem, the best comparisons are of side-by-side runs. The SiC + ice samples (Figure 8*a*) have steady state strengths that are indistinguishable from the well-established standard ice datum at $T = 223$ K. The one sample of $\phi = 0.20$ calcite + ice tested at 223 K had about the same strength as standard ice (Figure 8*a*). At lower temperatures, calcite + ice is also about 10% stronger than standard ice but only when compared with the recently deformed standard ice samples. The 10% higher strength was observed in each of the four side-by-side comparisons we made (Figures 3–5).

The three samples of coarse-grained ice had a slightly

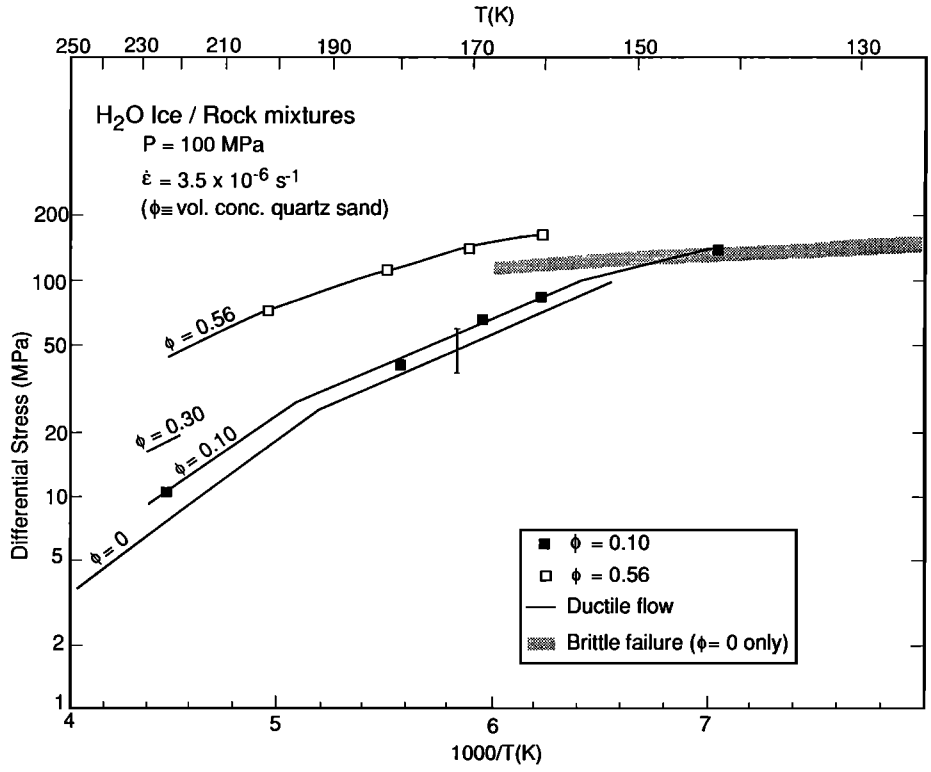

Fig. 9. Flow of ice + quartz sand as a function of particulate concentration, derived from the data in Figure 8*b*.

higher strength than standard ice in side-by-side comparisons (Figures 3 and 4), but it is difficult to say if this difference is significant. Fine-grained pure ice had about the same strength as standard ice (Figure 8*c*).

The contrast between quartz sand + ice and standard ice is distinct (Figure 8*b*). Even at $\phi = 0.10$, strengths are slightly but consistently higher than for $\phi = 0.20$ calcite + ice. The differences between quartz and calcite inclusions may be related to texture. As discussed later, the coarser quartz particulates do not form as uniform a network along ice grain boundaries as does the extremely fine calcite powder. At $\phi = 0.30$ the samples are more than twice as strong as standard ice, and at $\phi = 0.56$, close to the theoretical packing limit, the samples are 2–5 times as strong as standard ice, depending on temperature.

Steady state strength σ_{ss} levels in the $\phi = 0.56$ quartz + ice samples show a remarkable similarity to the strength of jacketed samples of St. Peter sand [*Borg et al.*, 1960], where strengths double when confining pressure is raised from 50 to 100 MPa. (The actual strength levels measured by Borg et al. were about 100 and 200 MPa at $\varepsilon = 0.20$; strain rates were not specified. We assume their strain rates were within an order or two of magnitude of ours.) Thus the differences between the two curves in Figure 6, especially after the initial yielding, may be partly a result of different confining pressures. Temperature-stepping tests at constant pressure (Table 1, runs 234 and 253) indicate that σ_{ss} retains a dependence on strain rate and/or temperature at $\phi = 0.56$. Quantitatively, we can say that the ratio Q^*/n for $\phi = 0.56$ quartz + ice is about 6 kJ/mol versus about 8 kJ/mol for pure ice at $T < 195$ K (Table 3). Data required to compute n directly (values of σ_{ss} at the same T but different $\dot{\varepsilon}$) are sparse and badly scattered (Figure 8*b*). The strength appears to be rather strain-rate-insensitive (n is high) compared with pure ice, judging qualitatively from the proximity in Figure 8*b* of symbols representing different strain rates; the low value of Q^*/n may be entirely due to a high value for n.

A simplified version of Figure 8*b* is redrawn in Figure 9 to illustrate the collective behavior of quartz sand + ice reduced to a common strain rate. The plot suggests a simple relationship between σ_{ss} and ϕ. The $\phi = 0.56$ samples may be anomalously strong because of contacting sand particles, as discussed in the previous section, although the fact that there is still a temperature dependence to their strength means that ice retains some influence. The flow law for a $\phi = 0.45$ sample would probably lie closer to that for a $\phi = 0.30$ than to that for a $\phi = 0.56$ sample in Figure 9.

Effect of particulates on faulting. The "shear instability limit" in Figures 7*a* and 8*b* marks the limit to which we can achieve flow without faulting in standard ice. The boundary is strain rate insensitive, and because of the unusual role of the phase transformation ice I → II in the instability, it is also pressure insensitive above $P = 50$ MPa [*Durham et al.*, 1983; *Kirby et al.*, 1991]. The barrier has been deeply penetrated by three of the quartz + ice samples. Two of these were $\phi = 0.56$ quartz and the other was a $\phi = 0.10$ sample that deformed in a ductile manner at $\sigma_{ss} = 141$ MPa at $T = 142 \pm 2$ K and $\dot{\varepsilon} = 3.5 \times 10^{-6}$ s^{-1}. The highest stress supported by a pure ice sample deforming in a ductile manner was $\sigma_{ss} = 111$ MPa (Figure 7*a*).

We should emphasize that this increased ductility is not a strengthening in the sense discussed in preceding paragraphs. Rather, the effect seems to be an increased toughness. One explanation for this behavior is the limiting of crack growth by sand particles, making a critical flaw length harder to achieve. To illustrate how pronounced this tough-

ening is, the behavior of the sample just cited contrasts with four samples tested in an earlier study [*Durham et al.*, 1983] at $T = 141 \pm 2$ K and $\dot{\varepsilon} \approx 3.5 \times 10^{-6}$ s^{-1}. All four showed a slight amount of ductility, in that the stress-strain curves showed a small but measurable departure from elasticity just before failure. However, all four did fail on a macroscopic shear fault in a narrow range of ultimate strengths from 126 to 136 MPa.

The three samples tested at 77 K actually did suffer unstable faulting (Table 1). Typical values of σ_u for pure ice at 77 K are 165 ± 10 MPa with occasional failure at lower stresses [*Durham et al.*, 1983], so the contrast in strengths between pure ice and mixed-phase ice is not significant. One distinct difference did occur in the manner of failure of the particulate + ice samples. Rather than being sudden, as with pure ice, the loss of strength marking the failure event was drawn out over 1–2 s.

Microstructural studies. The origin of the yield point and strain-softening behavior of pure ice was investigated in a series of four runs at 213 K, 3.5×10^{-4} s^{-1}, and confining pressure of 100 MPa that were halted and removed from the apparatus at four critical points along the stress-strain curve from initial yield to maximum stress to strain softening to steady state (Figure 2). Thin sections made from these samples show a progression of grain structures and texture. At the first step just before the σ_u maximum (Figure 10*a*), some of the grains show evidence of plastic deformation as indicated by internal rotation of the extinction position (undulatory extinction), a feature not seen in the starting material. Also, some grain boundaries are bowed rather than planar as in the starting material. At the peak stress (Figure 10*b*) about 20% of the grains show optical evidence for internal deformation and some suggestion of grain flattening is seen. The permanent macroscopic strain at these first two steps is 0.005 to 0.010. On the strain-softening part of the stress-strain curve beyond the peak (Figure 10*c*), now at $\varepsilon = 0.017$, grain size has increased dramatically and all optical evidence for internal grain deformation has disappeared. Approaching steady state, the sample taken to $\varepsilon = 0.057$ (Figure 10*d*) has a reduced grain size compared with that in Figure 10*c* with little or no undulatory extinction, and most grain boundaries are planar. Evidently, initial transient behavior is associated with the development of a recrystallized microstructure after an initial phase of plastic deformation and work hardening. As in some other minerals and nonmetallic compounds, continued recrystallization is likely to have the effect of reducing creep strengths by reducing dislocation glide interactions, in effect like a perpetual primary creep stage [see *Tullis and Yund*, 1985, 1987; *Gottstein and Mecking*, 1985]. The variability of the initial yield behavior between samples with identical grain size and among samples with different initial grain size evidently reflects variability in the nucleation of new grains. The presence of small amounts of SiC particles evidently removes this variability. Other pure ice samples taken to larger strain show no grain-shape anisotropy, indicating that recrystallization acts to keep grains equant during flow at large strain.

Ice with hard particulates shows textures that depend on the distribution of the hard phase. The starting material of $\phi = 0.20$ calcite has most of the calcite segregated in ice-calcite regions near original ice grain boundaries (Figure 1*b*), and their deformed counterparts show a partitioning of strain localized in the larger original ice grains that have recrystallized during deformation (Figure 11*a*). Many of the regions of calcite/fine-grained ice are not measurably thinner perpendicular to the compression direction, whereas the exclusively ice regions are recrystallized and the boundaries of the original grains indicate large shortening strains in the compression direction (Figure 11*b*). Measurements of the changes in shapes of the essentially pure ice and ice-calcite domains suggest a ratio of greater than 10 in average strain and strain rate between the pure ice regions and the fine-grained calcite-ice regions.

Indium jacket replicas of $\phi = 0.10$ and 0.30 quartz + ice samples also show textures dominated by elongate, deformed ice grains separated by regions of an ice/particulate mix (Figure 12). In quartz + ice deformed samples, however, there is a smaller contrast in strains between the pure ice regions and ice/particulate matrix compared with deformed calcite + ice samples. We suspect that this is due to the large difference between quartz and calcite grain sizes (100X) and the resultant far smaller number of quartz grains in the ice/particulate matrix.

Indium jacket replicas of $\phi = 0.56$ quartz + ice samples that were deformed at relatively low temperatures (<190 K) show remarkable lamellar features oriented normal to the compression direction and are nearly identical in appearance to ice II microinclusions observed in pure ice under similar conditions (Figure 13). These ice II inclusions crosscut and envelope quartz grains. *Kirby et al.* [1991] have shown that these inclusions form at a critical temperature-dependent limit of the maximum compressive stress (i.e., differential plus confining stress) when ice II microinclusions nucleate and grow at rates that accommodate the imposed strain rate via the 20% volumetric strain of the ice I → II transformation. Thus the strength of samples of ice + $\phi = 0.56$ quartz is influenced by two factors that exist in none of the other samples: an interconnected network of quartz grains, and the kinetics of the ice I → II phase transformation.

DISCUSSION

The foregoing experimental results should be interpreted in the context of the general effects of dispersed hard phases in composite materials. The effects can be far greater than expected from simple law-of-mixtures predictions. This is even true of suspensions of hard particles in Newtonian fluids, in which macroscopically non-Newtonian behavior and also nonlinear dependence of volume fraction ϕ on viscosity are observed [see, e.g., *Batchelor*, 1974; *Jeffrey and Acrivos*, 1976; *Friedson and Stevenson*, 1983]. Particles disturb the pattern of flow so that the fluid must travel around them, dissipating energy as viscous friction. Nonhydrodynamic forces, such as those due to particle electrical charges or Brownian motion in the fluid, can also act on particles and increase viscosity. In crystalline solids, particles, even voids, can disturb the pattern of flow by impeding the motion of crystal defects that govern the plastic rheologies of crystalline solids (see *Bilde-Sorensen* [1983] for a general review).

Strengthening of metals by dispersed hard inclusions is an important hardening process in engineering technology. Theory and experiments show that this strengthening is typically manifested as a threshold stress, below which strain rates rapidly approach zero. At low temperatures where plasticity

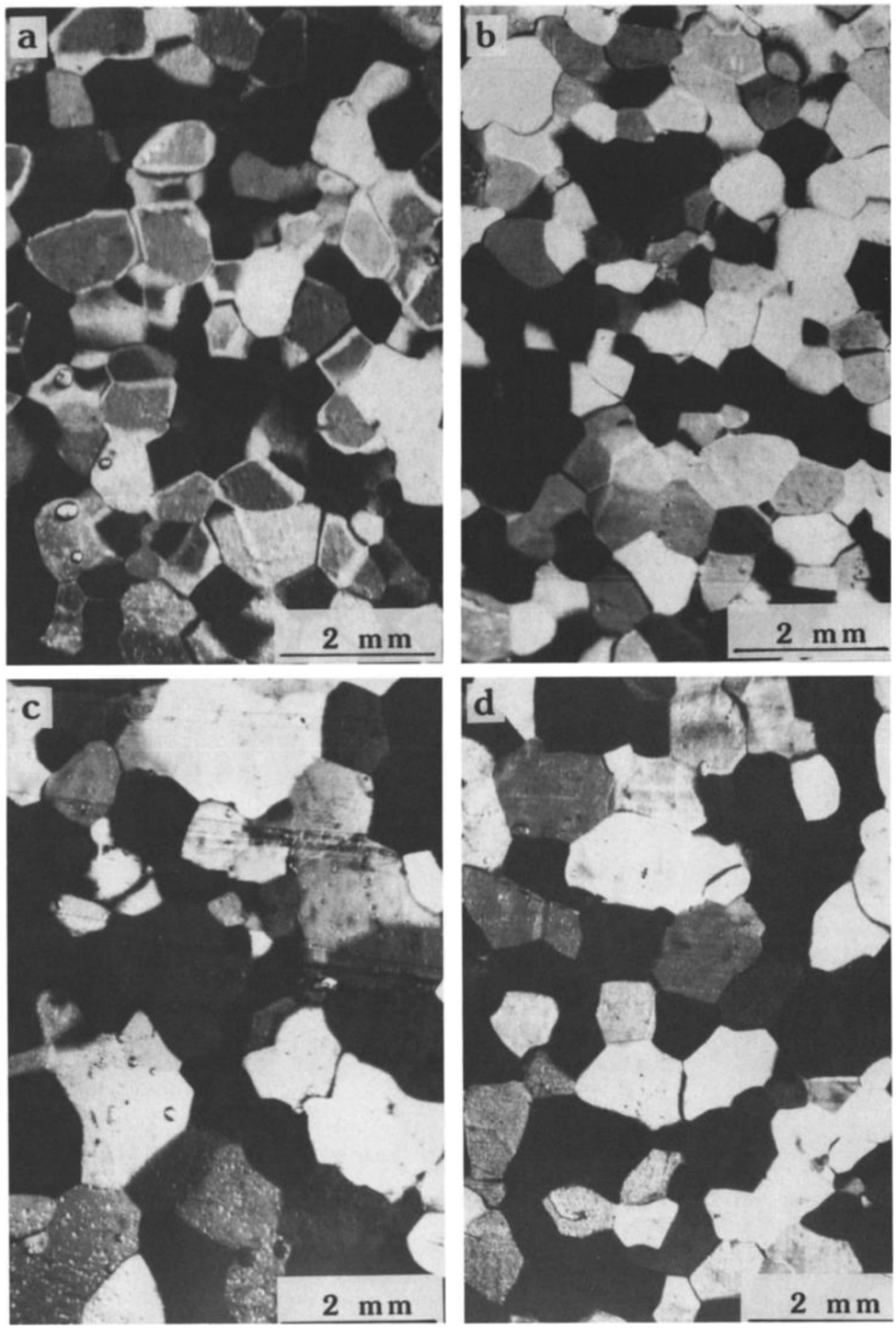

Fig. 10. Textural development in pure ice during transient deformation at $T = 213$ K, $P = 100$ MPa, and $\dot{\varepsilon} = 3.5 \times 10^{-4}$ s^{-1}. Figures are photomicrographs of thin sections viewed through crossed polarizers and are from samples strained to the points shown by the four arrows in Figure 2. (*a*) Permanent strain $\varepsilon = 0.0072 \pm 0.0016$, just prior to the strength maximum σ_u; (*b*) $\varepsilon = 0.0092 \pm 0.0016$, at σ_u; (*c*) $\varepsilon = 0.0168 \pm 0.002$, just beyond σ_u; and (*d*) $\varepsilon = 0.0569 \pm 0.002$, approaching steady state.

is generally governed by the glide motion of crystal dislocations, this threshold stress τ_0 is generally identified with the Orowan stress [*Orowan*, 1948], the stress required for dislocations to bow out sufficiently between particles that they can bypass them and thereby contribute to macroscopic plastic deformation. Orowan showed that τ_0 should be proportional to the dislocation line tension (equated with the dislocation line energy) and inversely proportional to the product of the Burgers vector magnitude b and the spacing D between the point obstacles in the slip plane. The Orowan theory has been refined since 1948, taking into account the effects of the finite particle diameter a and better estimates of the true obstacle spacing and line tension. A currently accepted form of the Orowan equation [*Ashby*, 1969; *Kelly*,

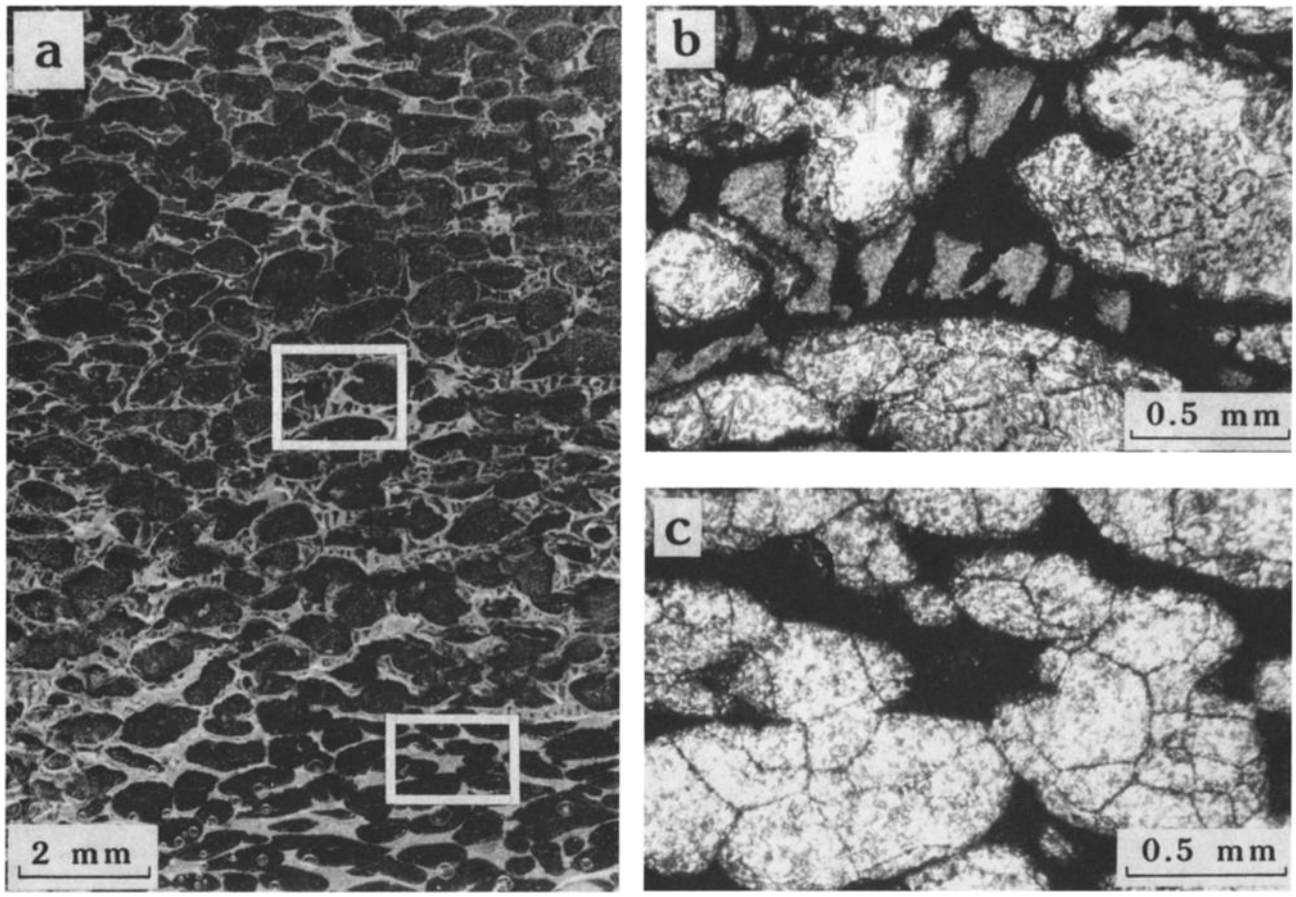

Fig. 11. (*a*) Reflected light micrograph of a replica of a polished surface of $\phi = 0.20$ calcite + ice sample 194, deformed to an average strain of 0.304 at 223 K, 50 MPa, and 3.5×10^{-4} s^{-1}. The strain in the central 3/5 of the sample, indicated mainly by the major-to-minor axis ratios of the dark elliptical shapes (the ice-rich domains), is about 0.50. The direction of applied stress was vertical in this section. (*b*) and (*c*) Magnifications of boxes outlined in Figure 11*a* taken in transmitted light, making icy regions bright and calcite-rich regions dark, the reverse of Figure 11*a*. The segregation of calcite and ice within the grain-boundary structures in Figure 11*b* is the result of extensional strain in the plane perpendicular to the compression axis. The recrystallization of ice within the original ice domains is apparent in Figure 11*c*. New ice grains measure 0.2–0.4 mm across and are approximately equant.

1973; *Lund and Nix*, 1976] that is in good agreement with low-temperature yield-stress data from metals is

$$\Delta\tau_0/\mu = \frac{0.83b \ln(a/r_0)}{2\pi(1-\nu)^{1/2}(D-a)}$$

where $\Delta\tau_0$ is the strength increment caused by the Orowan effect, μ is the shear modulus, ν is Poisson's ratio, and r_0 is the inner cutoff radius for the dislocation line energy calculation, usually taken to be $4b$ to $5b$. The planar interparticle spacing is $D = 1/(aN_v)^{1/2}$, where $N_v = 6\phi/\pi a^3$ is the number of particles per unit volume. We can estimate $\Delta\tau_0$ if, for the moment, we assume that the interparticle spacing is uniform. For ice, $\mu = 3800$ MPa, $\nu = 0.325$, and $b = 0.45$ nm under our experimental conditions, and we take $r_0 = 5b$. For the calcite + ice samples, $a = 2$ μm, $\phi = 0.2$, $N_v = 4.8 \times 10^{16}$ m^3, $D = 3.2$ μm and the Orowan stress is 1.6 MPa. A similar calculation for the SiC + ice samples gives $\Delta\tau_0 = 7$ Pa. For quartz sand + ice samples, $\Delta\tau_0 = 23$ kPa with $\phi = 0.10$. An assumption of the Orowan model that $D \gg a$ breaks down for the $\phi = 0.30$ and 0.56 samples.

These values of critical shear strength are too small to be resolved in our experiments and even these predictions of the threshold stress are overestimates for a number of reasons. First, the particulates are not uniformly distributed in our samples, reducing the Orowan strengthening effect [*Ashby*, 1969; *McClintock and Argon*, 1966] by allowing dislocations to move unimpeded in particle-free zones. Our method of growing all but the $\phi = 0.56$ samples resulted in segregation of the particulates to the boundary regions of the larger ice grains. For example, in the $\phi = 0.20$ calcite sample shown in Figure 1*b*, the larger, nearly calcite-free ice grains occupy 76 ± 2% of the volume. Our textural analysis indicated that the ratio of strain in the larger ice grains to that in the calcite-rich domains in the interstices was more than 10. This means that the effective strain rate in the nearly calcite-free ice is 0.76^{-1} times the bulk strain rate and the strengthening factor due to the larger effective strain rate is $0.76^{-1/n} = 1.07$ where $n = 4$ (Table 3), assuming a uniform state of stress exists throughout the aggregate [*Tullis et al.*, 1991]. This strengthening estimate is, within measurement uncertainty, in agreement with that observed in the calcite + ice samples (Figures 3–5). No additional strengthening process is required.

A second reason that the Orowan stress is an overestimate

is that at elevated temperatures, dislocations can break free of their Orowan barriers by dislocation climb, which shifts the threshold stress to lower values than the Orowan stress [*Lund and Nix*, 1976; *Hausselt and Nix*, 1977; *Honeycombe*, 1984]. The Orowan analysis also neglects the roles of grain boundaries in the macroscopic rheology of polycrystalline aggregates. Particulates can alter the mobility of grain boundaries similarly to the way they impede dislocation motion [*Bilde-Sorenson*, 1983; *Ashby*, 1980]. The central role of recrystallization in the strain softening of ice discussed earlier and the possible contributions of grain boundary sliding to creep suggest that strengthening well below the Orowan stress may occur due to grain boundary pinning.

Our test conditions do not overlap those of earlier experiments on the effects of hard particles on the strength of ice aggregates [*Nayar et al.*, 1971; *Hooke et al.*, 1972; *Baker and Gerberich*, 1979], so comparisons are difficult. These studies involved unconfined tests at high temperatures (238–271 K) under nominally constant axial stress. Creep rates were established over strain intervals generally less than 1%, and total strains were either unspecified or less than a few percent. Our experiments at elevated pressures indicate that the effects of particulates depend on whether transient or steady state behavior (at strains exceeding 10%) is being compared. *Hooke et al.* [1972] found higher creep rates, compared with pure ice, in ice samples with sand-sized particles at $\phi < 0.1$ and $T = 264$–266 K, especially during transient flow. This result is in qualitative agreement with the reduction of ultimate strength in some of our experiments. At larger volume fractions and lower temperatures, Hooke et al. found creep rates were reduced compared with pure ice. The study of *Baker and Gerberich* [1979] suffered from a large scatter in creep rates, especially when they are corrected for variations in test stress. In general, however, their particulate + ice aggregates crept at higher rates than pure ice at $T > 255$ K and at significantly reduced rates below that temperature. *Nayar et al.* [1971] molded samples with remarkably uniform distributions of 0.015-mm silica particles, but the sample grain sizes were neither controlled nor specified. Also, theirs were tensile tests, favoring even more microcracking and void formation than unconfined compressional tests. Nonetheless, samples with $\phi = 0.01$ were more creep resistant than pure ice and also more creep resistant than two samples with $\phi = 0.05$, suggesting a rather complex hardening effect. The values of a and ϕ in their

Fig. 13. Indium jacket replica of $\phi = 0.56$ quartz sand + ice sample 234, deformed to $\varepsilon = 0.257$ at 183 and 162 K, 100 MPa, and $\dot{\varepsilon} = 3.5 \times 10^{-5}$ s^{-1}. The long striations run normal to the stress direction and mark where ice I has transformed to the II phase, which is about 20% denser. The morphology of the ice II inclusions is typical of pure ice samples transformed from I to II under similar conditions of temperature and normal stress.

Fig. 12. Indium jacket replica of the surface of $\phi = 0.10$ quartz sand + ice sample 235, deformed to $\varepsilon = 0.260$ at 180 K, 100 MPa, and varying strain rates. Illumination is from the top, and the direction of applied stress was vertical. The domain structure is apparently the result of higher strain in the ice-rich regions (causing the elongate depressions in the replica).

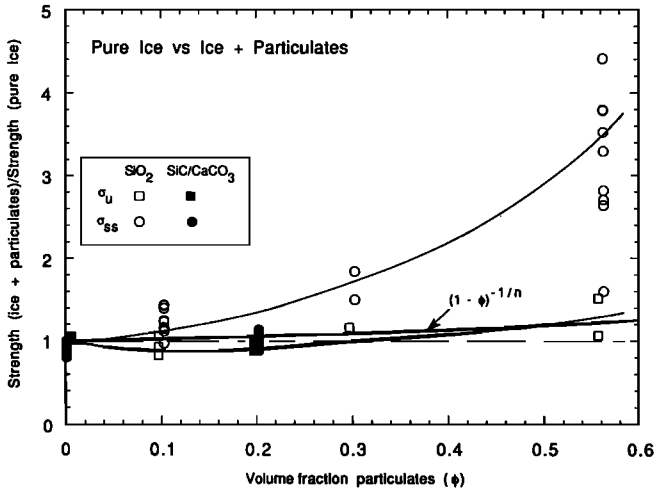

Fig. 14. Relative ultimate (squares) and steady state (circles) strengths for mixtures of ice + hard particulates as a function of volume concentration of particulates. The dashed line represents values for pure ice. Squares and circles are slightly staggered along the horizontal axis to avoid overlap. SiC + ice (at $\phi = 0.001$ exclusively) and calcite + ice (at $\phi = 0.20$ exclusively) share common symbols. The curve labeled $(1 - \phi)^{-1/n}$ is the strengthening expected on the basis of geometric considerations alone (see text). The heavier solid lines are estimated fits to the SiO_2 data.

samples were such that the predicted Orowan shear stress was more than a factor of 10 higher than the applied stress, demonstrating that at high temperatures, other factors control the strengthening effects of particulates.

An obvious limitation of the present work is that the molding technique for making all but the $\phi = 0.056$ quartz + ice samples produced heterogeneous particle distributions that probably reduced the overall effects of the particulates. This was most evident in the $\phi = 0.20$ calcite + ice samples, as noted above. Clearly, improvements in the methods for making samples are needed to achieve more uniform mixtures. Nevertheless, the sensitivity of strengthening to the spatial distribution of hard particles observed in this study suggests that particle heterogeneities in nature also tend to reduce the potential strengthening effects of hard second phases. Segregations of purer ice are likely regions of strain localization in steady state flow, whereas the opposite may be true at low permanent strain. Last, improvements are needed in the methods of optical examination of deformed samples, notably in the preparation of thin sections for petrographic study.

We summarize most of our mechanical results in Figure 14, which plots relative strength versus ϕ, where relative strength is defined as the ratio of the strength of a particulate + ice sample to that of a pure ice sample under identical or nearly identical conditions. Following the geometric argument made above for calcite + ice, the strain rate in the ice fraction of a mixture must be at least $(1 - \phi)^{-1}$ times the macroscopic strain rate, so the stress must be at least $\Psi = (1 - \phi)^{-1/n}$ [see also *Friedson and Stevenson*, 1983]. The function $\Psi(\phi)$ is also plotted in Figure 14. The relative ultimate strengths for samples of $\phi \leq 0.20$ are less than Ψ and slightly but significantly lower than unity, evidently showing the effects of particulates on the nucleation of new ice grains that our work demonstrates controls the onset of strain softening and the magnitude of σ_u. Samples with $\phi \geq 0.30$ have relative ultimate strengths comparable to Ψ.

In contrast, the steady state strength ratios are much too high (2.5 to 4.5) at $\phi = 0.56$ to explain by geometrical strengthening alone. The steep nonlinear rise in the relative steady state strength with increasing ϕ shown in Figure 14 probably reflects interaction of the flow field in the ice matrix around adjacent hard particles, helping support the load between hard particles even when the particles do not actually touch each other. Put another way, the hard particles evidently "feel" the nonlinear viscous stresses that attend concentrated ice deformation between them, even more than predicted by geometrical strengthening. As pointed out earlier, at $\phi = 0.56$, the steady state strength approaches that of dry confined sand [*Borg et al.*, 1960], suggesting direct contact of the hard particles. Relative strengths are scattered at $\phi = 0.56$ in Figure 14 due to a lower strain rate and/or temperature sensitivity relative to pure ice.

The $\phi = 0.20$ calcite + ice samples are an obvious departure from the regular increase of relative steady-state strength sketched in Figure 14. We have already noted the extreme segregation of the calcite to the matrix between large calcite-free domains (Figure 11). This segregation shifts relative strength to values comparable to the geometrical strengthening ratio Ψ.

IMPLICATIONS FOR PLANETOLOGY

The average values of ϕ for moons like Ganymede, which have mean densities near 2, must be 0.4–0.5. *Friedson and Stevenson* [1983] have calculated an expected range of viscosity ratios for Newtonian fluids using two empirical expressions that bound the relative viscosities in suspensions, and they predicted that relative viscosities should range from about 2.4 to 3.0 for suspensions with $\phi = 0.3$ and from 9.9 to 58 for those with $\phi = 0.6$. They also noted that these hydrodynamic strengthening effects of particulates in suspensions are expected to be smaller in suspensions in non-Newtonian ($n > 1$) fluids. Our steady state results for mixtures of hard particles + ice, ice being a material that is markedly non-Newtonian, indicate that viscosity ratios for these mixtures are larger than expected even for Newtonian fluids. For samples with $\phi = 0.30$ and 0.56, Figure 14 shows that relative steady state strengths are about 1.5 and 3.5, respectively, resulting in viscosity ratios of 5 and 150 (using $n = 4$). Thus the conjecture by Friedson and Stevenson that high-viscosity material will lead to excessive internal heating and melting actually becomes more likely. However, in considering the implication of these higher relative viscosities for the thermomechanical evolution of icy satellites, it is worth bearing in mind that predictions of the effects of particulates depend critically on how the particles are distributed.

A surface layer of ice and rock on Ganymede or Callisto that is 50% rock by volume will have a viscosity that is about 2 orders of magnitude higher than that of pure ice, if the results in Figure 14 extrapolate directly to planetary strain rates. (Note that the lowered effect of particulates in the transient stage of deformation, the lower curve in Figure 14, offsets the higher strength of pure ice in this stage, resulting in viscosity for rock + ice that is less strain-sensitive than that of pure ice.) The implications for retention of surface

topography are therefore favorable, but before our results can be used to estimate the particulate content of surface ices, the differences between models of surface processes (e.g., *Croft* [1988] and *Thomas and Schubert* [1988] versus *Schenk* [1991] and *Hillgren and Melosh* [1989]) will have to be resolved.

Acknowledgments. We thank M. A. Daley for thin sectioning and photographing the ice samples shown in Figure 10 and K. A. Ragaini for her assistance in conducting the experiments. NASA support under order W-15,070 is gratefully acknowledged. This work was performed under the auspices of the U.S. Department of Energy by the Lawrence Livermore National Laboratory under contract W-7405-ENG-48.

REFERENCES

Ashby, M. F., On the Orowan stress, in *Physics of Strength and Plasticity*, edited by A. S. Argon, pp. 113–131, MIT Press, Cambridge, Mass., 1969.

Ashby, M. F., The influence of particles on boundary mobility, in *Recrystallization and Grain Growth of Multiphase and Particle Containing Materials*, edited by N. Hansen, A. R. Jones, and T. Leffers, pp. 325–336, Riso National Laboratory, Roskilde, Denmark, 1980.

Baker, R. W., The influence of ice-crystal size on creep, *J. Glaciol.*, *21*, 485–500, 1978.

Baker, R. W., and W. W. Gerberich, The effect of crystal size and dispersed-solid inclusions on the activation energy for creep of ice, *J. Glaciol.*, *24*, 179–194, 1979.

Batchelor, G. K., Transport properties of two-phase materials with random structure, *Annu. Rev. Fluid Mech.*, *6*, 227–255, 1974.

Bilde-Sorensen, J. B., Creep of particle-containing materials, in *Proceedings of the 4th Riso International Symposium on Metallurgy and Materials Science*, edited by J. B. Bilde-Sorensen et al., pp. 1–14, Riso National Laboratory, Roskilde, Denmark, 1983.

Borg, I., M. Friedman, J. Handin, and D. V. Higgs, Experimental deformation of St. Peter sand: a study of cataclastic flow, in Rock Deformation, edited by D. Griggs and J. Handin, *Mem. Geol. Soc. Am.*, *79*, 133–191, 1960.

Croft, S. K., Crater/diameter/morphology relationships on the icy satellites: Implications for ice rheology, *Lunar Planet. Sci.*, *XIX*, 219–220, 1988.

Durham, W. B., H. C. Heard, and S. H. Kirby, Experimental deformation of polycrystalline H_2O ice at high pressure and low temperature: Preliminary results, *Proc. Lunar Planet. Sci. Conf. 14th*, Part 1, *J. Geophys. Res.*, *88*, suppl., B377–B392, 1983.

Friedson, A. J., and D. J. Stevenson, Viscosity of rock-ice mixtures and applications to the evolution of ice satellites, *Icarus*, *56*, 1–14, 1983.

Geissler, P. E., and S. K. Croft, Dispersion hardening of ice: Implications for topographic relaxation on the icy satellites, *Lunar Planet. Sci.*, *XIX*, 381–382, 1988.

Gottstein, G., and H. Mecking, Recrystallization, in *Preferred Orientation in Deformed Rocks: An Introduction to Modern Texture Analysis*, edited by H.-R. Wenk, pp. 183–218, Academic, San Diego, Calif., 1985.

Hausselt, J. H., and W. D. Nix, A model for high-temperature deformation of dispersion strengthened metals based on substructural observations in Ni-20Cr-$2ThO_2$, *Acta Metall.*, *25*, 1491–1502, 1977.

Heard, H. C., W. B. Durham, C. O. Boro, and S. H. Kirby, A triaxial deformation apparatus for service at $77 \leq T \leq 273$ K, in *The Brittle-Ductile Transition in Rocks*, *Geophys. Monogr. Ser.*, vol. 56, edited by A. G. Duba, W. B. Durham, J. W. Handin, and H. F. Wang, pp. 225–228, AGU, Washington, D. C., 1990.

Hillgren, V. J., and H. J. Melosh, Crater relaxation on Ganymede: Implications for ice rheology, *Geophys. Res. Lett.*, *16*, 1339–1342, 1989.

Honeycombe, R. W. K., *The Plastic Deformation of Metals*, 2nd ed., pp. 180–198, Edward Arnold, Baltimore, Md., 1984.

Hooke, R. LeB., B. B. Dahlin, and M. T. Kauper, Creep of ice containing dispersed fine sand, *J. Glaciol.*, *11*, 327–336, 1972.

Jeffrey, D. J., and A. Acrivos, The rheological properties of suspensions of rigid particles, *AIChE J.*, *22*, 417–432, 1976.

Kelly, P. M., The quantitative relationship between microstructure and properties in two-phase alloys, *Int. Metall. Rev.*, *18*, 31–36, 1973.

Kirby, S. H., W. B. Durham, M. L. Beeman, H. C. Heard, and M. A. Daley, Inelastic properties of ice Ih at low temperatures and high pressures, *J. Phys.*, *48*, suppl., 227–232, 1987.

Kirby, S. H., W. B. Durham, and L. A. Stern, Mantle phase changes and deep-earthquake faulting in subducting lithosphere, *Science*, *252*, 216–225, 1991.

Lund, R. W., and W. D. Nix, High temperature creep of Ni-20Cr-$2ThO_2$ single crystals, *Acta Metall.*, *24*, 469–481, 1976.

McClintock, F. A., and A. S. Argon, *Mechanical Behavior of Materials*, pp. 157–158, Addison-Wesley, Reading, Mass., 1966.

McKinnon, W. B., Geology of icy satellites, in *Ices in the Solar System*, edited by J. Klinger et al., pp. 829–856, D. Reidel, Norwell, Mass., 1985.

McKinnon, W. B., and E. M. Parmentier, Ganymede and Callisto, in *Satellites*, edited by J. A. Burns and M. S. Matthews, pp. 718–763, University of Arizona Press, Tucson, 1986.

Mueller, S., and W. B. McKinnon, Three-layered models of Ganymede and Callisto: Compositions, structures, and aspects of evolution, *Icarus*, *76*, 437–464, 1988.

Nayar, H. S., F. V. Lenel, and G. S. Ansell, Creep of dispersions of ultrafine amorphous silica in ice, *J. Appl. Phys.*, *42*, 3786–3789, 1971.

Orowan, E., Discussion, in *Symposium on Internal Stress in Metals and Alloys*, p. 451, Institute of Metals, London, 1948.

Parameswaren, V. R., and S. J. Jones, Triaxial testing of frozen sand, *J. Glaciol.*, *27*, 147–155, 1981.

Schenk, P. M., Ganymede and Callisto: Complex crater formation and planetary crusts, *J. Geophys. Res.*, *96*, 15,635–15,664, 1991.

Thomas, P. J., and G. Schubert, Power law rheology of ice and the relaxation style and retention of craters on Ganymede, *J. Geophys. Res.*, *93*, 13,755–13,762, 1988.

Tullis, J. A., and R. A. Yund, Dynamic recrystallization of feldspar: A mechanism of ductile shear zone formation, *Geology*, *13*, 238–241, 1985.

Tullis, J. A., and R. A. Yund, Transition from cataclastic creep dislocation creep of feldspar: mechanisms and microstructures, *Geology*, *15*, 606–609, 1987.

Tullis, T. E., F. G. Horowitz, and J. Tullis, Flow laws of polyphase aggregates from end-member flow laws, *J. Geophys. Res.*, *96*, 8081–8096, 1991.

W. B. Durham, L-201, Lawrence Livermore National Laboratory, P.O. Box 808, Livermore, CA 94550.

S. H. Kirby and L. A. Stern, U.S. Geological Survey, MS 977, 345 Middlefield Road, Menlo Park, CA 94025.

(Received March 2, 1992;
revised October 1, 1992;
accepted October 1, 1992.)